Journal of
Synchrotron Radiation

ISSN 0909-0495

Received 26 January 2011
Accepted 24 June 2011

Nanocomposite characterization on multiple length scales using μSAXS

Ruipeng Li,[a,b] Sterling Cornaby,[a,c] Marleen Kamperman[a,d] and Detlef-M. Smilgies[a]*

[a]Cornell High Energy Synchrotron Source, Cornell University, Ithaca, NY 14853, USA, [b]University of Science and Technology of China and National Synchrotron Radiation Laboratory, Hefei, Anhui 230029, People's Republic of China, [c]School of Applied and Engineering Physics, Cornell University, Ithaca, NY 14853, USA, and [d]Department of Materials Science and Engineering, Cornell University, Ithaca, NY 14853, USA. E-mail: dms79@cornell.edu

Nanocomposites have great potential for the rational synthesis of tailored materials. However, the templating process that transfers the self-organized nanostructure of a block copolymer or other mesophase onto the functional material is by no means trivial, and often involves multiple steps, each of which presents its own chemical and physical challenges. As a result the nanocomposite may not be homogeneous, but can be phase-separated into various components which may feature their own specific microstructure. Here it is shown how scanning microbeam small-angle X-ray scattering (μSAXS) can be used to characterize a thermoset resol/poly(isoprene-*block*-ethylene oxide) nanocomposite on multiple length scales with respect to homogeneity and microphase separation.

Keywords: X-ray microbeams; small-angle scattering; polymer microstructure; nanocomposites.

1. Introduction

Nanocomposites offer the potential of synthesizing novel materials with tailored nanostructures and functionalities (Bockstaller *et al.*, 2005; Hillmyer, 2005; Wan & Zhao, 2007). Prominent applications include nanoporous high-internal-surface-area material used for photovoltaics (Crossland *et al.*, 2009), catalysts (Kamperman *et al.*, 2009) or nanofiltration (Du *et al.*, 2004). The idea is to transfer the self-organized nanostructure of a block copolymer or silica mesophase onto a functional material, such as dye molecules or nanoparticles for light harvesting in dye-sensitized solar cells.

A nanocomposite typically consists of a nanostructured matrix, often a block copolymer with a specific morphology (lamellae, cylinders, spheres, bicontinuous phases) and a functional additive which preferentially swells one of the blocks. Further processing steps such as chemical and thermal curing (Hillmyer *et al.*, 1997; Lipic *et al.*, 1998), or calcination/pyrolysis (Du *et al.*, 2004; Crossland *et al.*, 2009), or photo-induced crosslinking and photolysis (Du *et al.*, 2004) may follow. Challenges in nanocomposite design are identifying a suitable chemically compatible template polymer for the desired functional additive, while taking into account the swelling of the block that the additive preferentially targets. This swelling may cause a transition to different block copolymer morphologies (Garcia *et al.*, 2009). Hence the block copolymer has to be carefully selected and designed.

In addition, processing conditions are often critical in order to achieve a homogeneous material and prevent heterogeneous morphologies or macrophase separation. For this reason a probe that is capable of characterizing the morphology of the composite on both the nanometer and on the micrometer scale is very useful (Riekel, 2000). Such information may provide clues on how to optimize the processing conditions. In the following we will show that small-angle X-ray scattering with an X-ray microbeam (μSAXS) can be utilized to study the morphology on multiple length scales and identify heterogeneous morphologies.

2. Experimental details

2.1. Materials

The poly(isoprene-*block*-ethylene oxide), PI-*b*-PEO, block copolymer was synthesized using standard anionic polymerization. The resulting polymer had a molecular weight of 22800 g mol^{-1} and 15.5 wt% PEO with polydispersity index of 1.02 as determined by gel-permeation chromatography (GPC) and proton nuclear magnetic resonance (^{1}H NMR). Resol, a phenolic resin, was synthesized following a recently reported procedure (Meng *et al.*, 2005, 2006). The molecular weight of resol was $\sim$300 g mol^{-1} based on GPC measurements. After 0.1 g of block copolymer was dissolved in tetrahydrofuran, 0.4 g of resol was added and stirred for 1 h at room temperature. The solution was poured into a Petri dish and a film was cast by solvent evaporation on a hot plate at 323 K for 3 h. The film was subsequently cured at 373 K for 24 h to crosslink the low-molecular-weight resol additive.

2.2. Scanning microbeam SAXS

An intense X-ray microbeam was prepared at the D1 beamline of the Cornell High Energy Synchrotron Source (CHESS). D-line features a high incoming X-ray flux of 10^{12} photons s^{-1} mm^{-2} from a multilayer monochromator comprising double-bounce Mo:B_4C multilayers with a 30 Å period. The multilayers defined an X-ray beam of 10 keV photon energy with a 1.5% bandwidth (Kazimirov *et al.*, 2006).

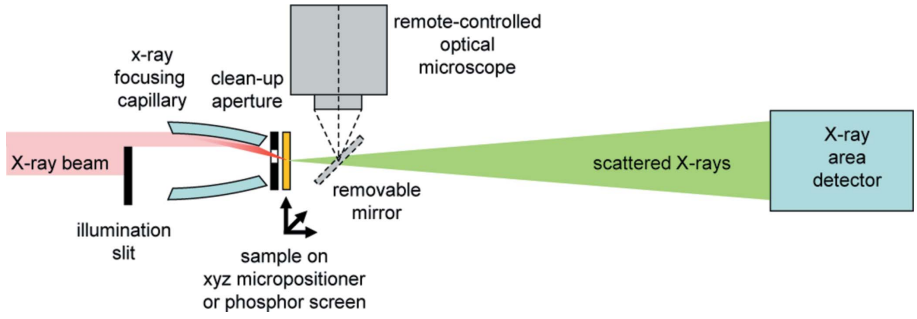

Figure 1
μSAXS scattering set-up at CHESS D1 station. For explanations see text.

The beam illuminates a single-bounce X-ray focusing capillary with an angular acceptance of 9 mrad and a working distance of 55 mm (Cornaby *et al.*, 2006). In order to reduce the divergence of the focused beam, and thus increase the SAXS resolution, only a 10% sector of the full accepted annulus was selected with incident beam slits upstream of the focusing capillary (Lamb *et al.*, 2007). A 5 μm pinhole or, alternatively, a high-resolution fluorescent screen in combination with a remote-controlled optical microscope (Navitar Machine Vision) and a removable 45° optical deflection mirror, were used to identify the location of the X-ray focus on-axis and to position the sample in the microbeam. A 200 μm clean-up aperture directly in front of the sample removed parasitic scattering from the tip of the X-ray focusing capillary (Lamb *et al.*, 2007). All components were lined up using Newport micropositioners with an accuracy of 1 μm. For an illustration, see Fig. 1.

The described set-up produced a 10 μm [horizontal (H)] × 15 μm [vertical (V)] X-ray focal spot (FWHM), as characterized by a scan of the X-ray focus with the 5 μm pinhole shown in Figs. 2(*a*) and 2(*b*). At the detector, a fiber-coupled CCD camera at a distance of 1900 mm from the sample position in the focal spot of the optics, the direct beam had a size (FWHM) of 3.4 mm (H) × 2.5 mm (V) (see Fig. 2*c*). This size translates to a beam divergence of 1.8 mrad (H) × 1.3 mrad (V). The microfocused beam showed some fine structure in the far-field image which is related to figure errors in the focusing capillary (Cornaby *et al.*, 2006). The center of mass of the beam far-field image was used to define the direct beam position (see Fig. 2). The flux in this microbeam was determined with an ion chamber as 1.3×10^{10} photons s^{-1}.

The angular divergence $\Delta(2\theta)$ owing to focusing at the sample position can be transformed into scattering vector smearing Δq with the usual formula

$$\Delta q = \frac{4\pi}{\lambda}\cos(2\theta/2)\,\Delta(2\theta)/2. \qquad (1)$$

For the evaluation we used the geometric mean of the horizontal and vertical divergence yielding $\Delta(2\theta) = 1.5$ mrad. The largest scattering angle intercepted by the camera is 1.2°, and thus Δq amounts to 0.08 nm^{-1}. Using this smearing value in conjunction with the Scherrer formula (Smilgies, 2009), the maximum resolvable grain size $R_{max} = 2\pi/\Delta q$ corresponds to 75 nm.

Another figure of merit is the minimum obtainable scattering vector q_{min} which is given by the size of the beam stop. The beam stop in the μSAXS camera had a diameter of 10 mm, in order to ensure that the full far-field image of the beam was covered (see Fig. 2*c*). In order to discern a scattering ring close to the beamstop, it should be at least 20 pixels or 1 mm away from the edge of the beamstop. This yields a minimum scattering vector of $q_{min} = 0.16$ nm^{-1}, which corresponds to a maximum resolvable *d*-spacing of $d_{max} = 39.3$ nm. The wavevector smearing was sufficiently small that adjacent scattering peaks of such a *d*-spacing can still be separated, and hence we expect the set-up to resolve structures with a period of up to about 40 nm.

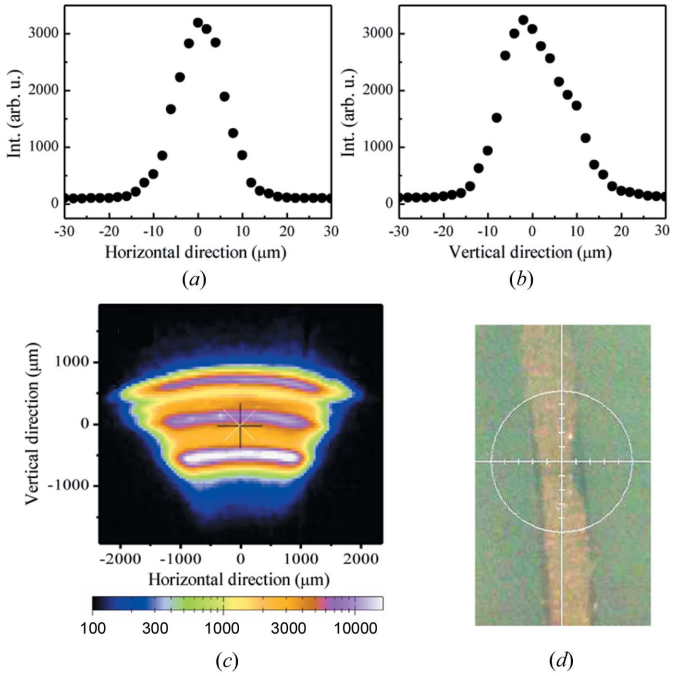

Figure 2
μSAXS characteristics. Horizontal (*a*) and vertical (*b*) pinhole scans of the focus. Taking the 5 μm pinhole size into account, the beam size was 10 μm (H) × 14 μm (V) FWHM. Flux at the focus was 1.3×10^{10} photons s^{-1}. (*c*) Far-field image of the microbeam on the CCD detector. The crosshair marks the center of mass of the intensity distribution. Beam divergence was determined to be 1.3 mrad (H) × 1.8 mrad (V) based on the far-field beam size. (*d*) Image of the sample in the line-up microscope. The crosshair marks the beam position. A tick mark corresponds to 10 μm.

The pixel size of the detector of 47 μm (H) × 47 μm (V) was not a limiting factor in our set-up. At a distance of 1900 mm from the sample this pixel size corresponds to an angular resolution of 25 μrad in either direction, which is much smaller than the beam divergence. In this regard our set-up is quite different from the microbeam scattering set-up developed by Riekel (2000) for combined SAXS/WAXS studies, where the detector is much closer to the sample and the pixel size becomes an important issue for the SAXS resolution. One of the goals of this study was to explore the theoretical limit of overall resolution, and as such we chose to use a traditional SAXS set-up in order not to be limited by the detector.

3. Results

Originally we became interested in the resol/PI-*b*-PEO nanocomposite as a test sample, because initial SAXS data, with a conventional 0.5 mm × 0.5 mm beam size, showed anisotropic powder rings (Fig. 3*a*). The scattering signal was dependent on the particular spot on the sample, indicating macroscale inhomogeneities. Hence it would have been very challenging to determine the structure of the different regions of the nanocomposite with standard SAXS analysis.

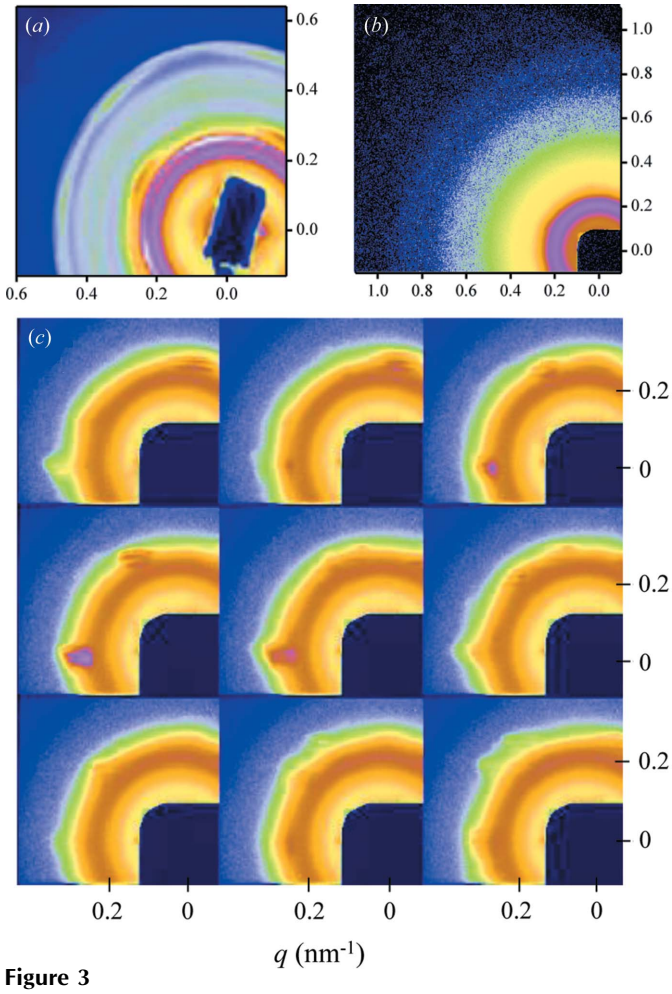

Figure 3
Typical SAXS images of the phase-separated PI-*b*-PEO/resol nanocomposite: (*a*) conventional SAXS using a 0.5 mm × 0.5 mm beam. (*b*) μSAXS image without scattering from inclusions. (*c*) 3 × 3 mesh scan of the sample with a step size of 10 μm both horizontally and vertically.

The optical appearance of the material was grayish opaque, indicating either macrophase separation or a heterogeneous morphology; in contrast, a homogeneous nanocomposite is expected to be transparent (Lipic *et al.*, 1998; Meng *et al.*, 2005). In a macrophase separated system the resol demixes from the block copolymer resulting in regions with pure resol and regions with pure block copolymer (Kosonen *et al.*, 2002; Sinturel *et al.*, 2007). In nanocomposites with a heterogeneous morphology, two or more nanocomposite morphologies coexist (Lipic *et al.*, 1998). The whole system is composed of microphase separated nanocomposite, but different regions have different morphologies. We decided to perform a μSAXS study in order to try to unravel the various components and length scales in the material.

For the μSAXS measurements we cut a 100 μm-thick slab of the composite material and probed it with the X-ray microbeam in about 200 different locations. Typical exposure times for single μSAXS images were of the order of 30 s. The scan images in Fig. 3(*c*) show that distinct crystalline inclusions featuring a different lattice spacing as compared with the matrix gave rise to the complications in the conventional SAXS image. Moreover, being able to obtain images from single inclusions with scanning μSAXS, we found that their scattering patterns featured hexagonal sets of reflections. While Fig. 3(*c*) shows a two-dimensional scan (step size 10 μm) of scattering from a single inclusion, we also obtained a few images from sample spots with no inclusion scattering (Fig. 3*b*).

The images collected without inclusion scattering were used to carefully characterize the matrix material. Our analysis in Fig. 4(*b*) shows the regularly spaced diffraction maxima characteristic of a lamellar structure with a lamellar period of 31.6 nm. Both even and odd peaks appeared, indicating asymmetric lamellae. The matrix scattering featured a homogeneous powder ring; hence the matrix consisted of grains of ordered domains oriented randomly with respect to each other. The radial width of the lamellar peaks was resolution limited, a side-effect of the divergence of the microfocused X-ray beam, as discussed above. However, based on the smooth appearance of the powder ring, the grain size had to be significantly smaller than 10 μm.

The two-dimensional patterns of the pure matrix scattering were used to subtract the matrix scattering from the more complex patterns containing one or multiple inclusions, and thus to highlight the scattering from individual inclusions. This way we obtained an azimuthally averaged radial scan of the inclusion scattering (Fig. 4*c*) which showed that the inclusions scattering patterns were consistent with a hexagonal cylinder morphology as given by the characteristic sequence $1 : \sqrt{3} : 2$ of relative spot positions and a *d*-spacing of 29.7 nm.

We contrast these findings with the integrated intensity from the conventional SAXS image in Fig. 4(*a*), from which the various components cannot be clearly discerned from each other. Using μSAXS, azimuthal scans of single inclusions showed that diffraction peaks of the same *q*-value had a 60°

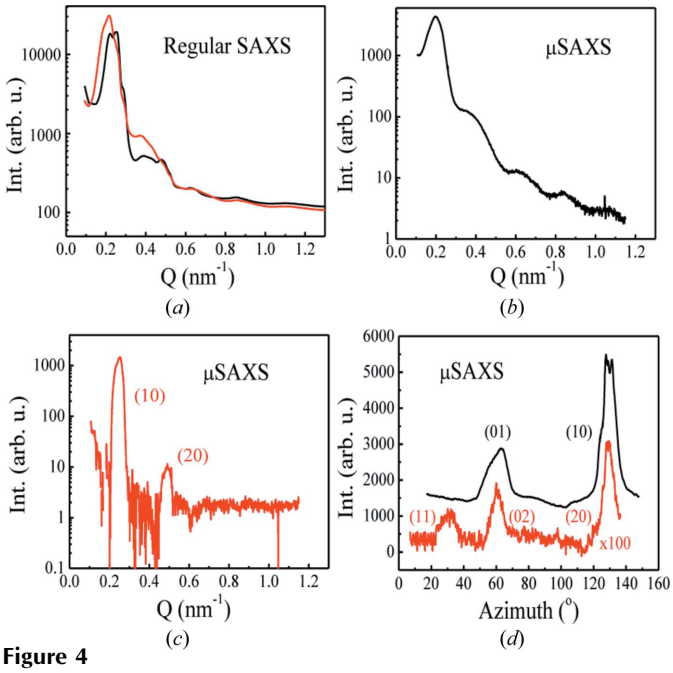

Figure 4
Morphology of matrix and inclusions. (*a*) Integrated regular SAXS patterns at two locations on the sample. (*b*) Integrated μSAXS pattern of the matrix only. Five orders of scattering from the lamellar structure can be discerned. (*c*) Integrated μSAXS pattern of the inclusions with the matrix subtracted. (*d*) μSAXS azimuthal scans radially integrated over the (10) reflection (top curve) as well as for the (11) and (20) reflections (bottom curve). The angular spacing between peaks of 60° and 30° clearly shows that this scattering signal is due to a hexagonal single-crystalline domain. The top curve was offset by 1500 for clarity. Note that the bottom curve was multiplied by a factor of 100.

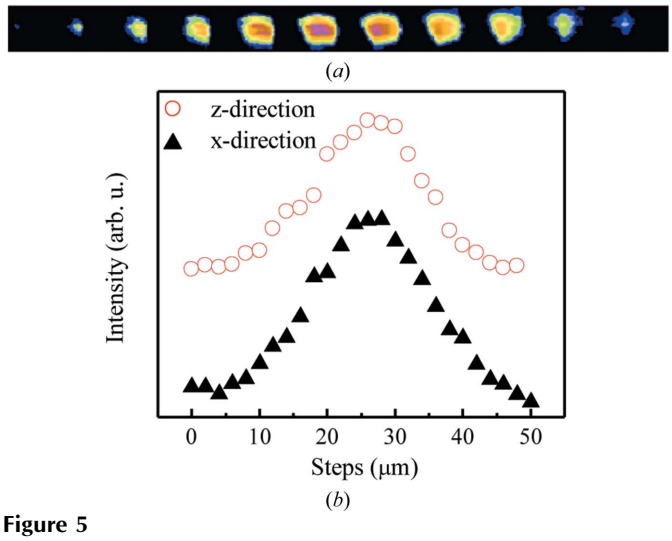

Figure 5
Determination of the inclusion size. (*a*) A series of CCD images of a single diffraction spot as a function of horizontal position. (*b*) Integrated intensities from a scan as shown on top. Horizontal inclusion size was 14.2 nm, vertical size was 12.1 nm.

spacing, and that the (11) peak had a 30° angle with the (10) peak (Fig. 4*d*). These findings corroborate our assessment of the single inclusions being in the hexagonal cylinder phase. Moreover, these results also indicate that such inclusions are single crystalline. Even in images with scattering from multiple inclusions in the microbeam, pairs of diffraction spots with the tell-tale 60° angular spacing could be identified.

The inclusion scattering spots in matrix-subtracted images could be used to determine typical inclusion sizes. To this end we scanned the sample in 5 μm steps close to a sample location producing a clean single inclusion image, both in the horizontal and the vertical direction. Fig. 5 shows the integrated intensity of a strong reflection plotted against the horizontal and vertical displacement. Taking the finite beam size into account, as determined above, the inclusion size could be determined as 14.2 μm horizontally and 12.1 μm vertically, *i.e.* the inclusion size was of the same size as the focal size of the microbeam.

We note that the diffraction spots from the single-crystalline inclusions replicated the fine-structure of the direct beam, as given by imperfections of the focusing optics. If we compare the appearance of such a spot with the image of the direct beam, we can conclude that the inclusion size has to be more or less similar to the focus size of the X-ray beam of 10 μm × 15 μm, in good agreement with the quantitative analysis described in the previous paragraph. Hence we have a simple means of telling the inclusion sizes observed at other sample locations. All single inclusion scattering features fell into the same size range of 10–15 μm.

4. Discussion

Our μSAXS data revealed a rich amount of detail of the nanocomposite morphology and coexistence of phases, both on the mesoscale as given by the microphase separation of the block copolymer as well as on the micrometer scale of the typical inclusion size. We found that for both the matrix and inclusions the respective structures were well resolved and we estimate experimentally that our set-up has a resolution of 40 nm, consistent with the theoretical estimate.

Mixing the resol with the amphiphilic block copolymer PI-*b*-PEO at a weight ratio of 4:1 is expected to lead to preferential swelling of the hydrophilic PEO domain with resol owing to their matching polarity. In the resulting microphase separated nanocomposite, resol and PEO are anticipated to form the majority domain and the PI block the minority domain (Hillmyer *et al.*, 1997; Lipic *et al.*, 1998). In contrast to our sample, Hillmyer and co-workers did not find signs of a heterogeneous morphology. Also in the work of Meng *et al.* (2005, 2006), which inspired our synthesis, heterogeneous morphologies were not reported.

Our scattering results indicate that the nanocomposite sample studied consisted of a matrix with lamellar morphology with a *d*-spacing of 31.6 nm as well as of inclusions with a hexagonal cylinder morphology with a *d*-spacing of 29.7 nm (see schematic in Fig. 6), corresponding to a nearest-neighbor distance of 34.3 nm. Morphology diagrams established for similar systems indicate that homogeneous nanocomposites consisting of 80 wt% resol in a block copolymer with 15.5 wt% PEO are expected to form an inverse hexagonal cylinder morphology with the PEO/resol forming the majority domain (Garcia *et al.*, 2009). It appears that the observed inclusions formed the expected hexagonal morphology.

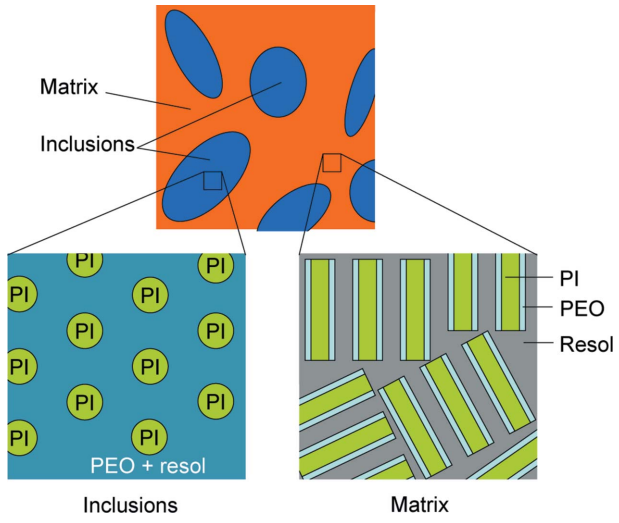

Figure 6
Structure model of the phase separated nanocomposite. Lamellar matrix of the resol/PI-*b*-PEO nanocomposite with inclusions of resol/PI-*b*-PEO nanocomposite in the hexagonal cylinder phase. The size of the inclusions of 10–15 µm is typical for the grain size in well ordered block copolymers. The grain size within the matrix could not be resolved by scanning.

The matrix seems to feature a lamellar morphology, consisting of small lamellar domains. It is not immediately obvious why this morphology was obtained and systematic changes of the synthesis protocol as well as additional experiments (*e.g.* differential scanning calometry, transmission electron microscopy) will be needed to provide conclusive answers. A phase coexistence region is expected between the lamellar phase and the inverted cylinder phase (Lipic *et al.*, 1998). Another possible driving force for a lamellar morphology is the tendency of PEO to crystallize below 323 K over a wide range of compositions and to form lamellar sheets of crystalline PEO (Zhu *et al.*, 2000; Floudas *et al.*, 2001; Kamperman *et al.*, 2008; Darko *et al.*, 2009).

Using SAXS measurements with an X-ray microbeam we were able to characterize the structure, morphology and average inclusion size in a heterogeneous PI-*b*-PEO/resol nanocomposite. Both micrometer-sized inclusions and fine-grained matrix were found to be microphase-separated on the mesoscale. Scanning µSAXS provides a unique opportunity of characterizing such materials on a variety of length scales and could be applied to guide the way to improve synthesis procedures.

RL acknowledges a fellowship from the Chinese Scholarship Council (CSC) for his stay at CHESS. MK acknowledges the support of the National Science Foundation (award DMR-0605856) and of the US Department of Homeland Security (Cooperative Agreement Number 2009-ST-108-LR0006). We thank Professors G. Pan (USTC and NSRL), Sol Gruner (Cornell and CHESS) and Ulrich Wiesner (Cornell) for their support. We are indebted to Jinwoo Lee, Cornell Materials Science and Engineering, for providing a nanocomposite test sample. We thank Richard Gillilan and Dave Schuller from the MacCHESS group for the use of their crystal centering software and for their help in calibrating the sample microscope. We thank Don Bilderback (CHESS) and Ulrich Wiesner (Cornell) for commenting on the manuscript. We greatly appreciate the support of the CHESS X-ray optics monocapillary group of Tom Szebenyi, Heong Soo and Don Bilderback. This work was conducted at the Cornell High Energy Synchrotron Source (CHESS) which is supported by the National Science Foundation and the National Institutes of Health/National Institute of General Medical Sciences under NSF award DMR-0225180.

References

Bockstaller, M. R., Mickiewicz, R. A. & Thomas, E. L. (2005). *Adv. Mater.* **17**, 1331–1349.
Cornaby, S., Szebenyi, T., Huang, R. & Bilderback, D. H. (2006). *Adv. X-ray Anal.* **50**, 194–200.
Crossland, E. J., Kamperman, M., Nedelcu, M., Ducati, C., Wiesner, U., Smilgies, D. M., Toombes, G. E., Hillmyer, M. A., Ludwigs, S., Steiner, U. & Snaith, H. J. (2009). *Nano Lett.* **9**, 2807–2812.
Darko, C., Botiz, I., Reiter, G., Breiby, D. W., Andreasen, J. W., Roth, S. V., Smilgies, D.-M., Metwalli, E. & Papadakis, C. M. (2009). *Phys. Rev. E*, **79**, 041802.
Du, P., Li, M., Douki, K., Li, X., Garcia, C. B. W., Jain, A., Smilgies, D.-M., Fetters, L. W., Gruner, S. M., Wiesner, U. & Ober, C. K. (2004). *Adv. Mater.* **16**, 953–957.
Floudas, G., Vazaiou, B., Schipper, F., Ulrich, R., Wiesner, U., Iatrou, H. & Hadjichristidis, N. (2001). *Macromolecules*, **34**, 2947–2957.
Garcia, B. C. W., Kamperman, M., Ulrich, R., Jain, A., Gruner, S. M. & Wiesner, U. (2009). *Chem. Mater.* **21**, 5397–5405.
Hillmyer, M. A. (2005). *Adv. Polym. Sci.* **190**, 137–181.
Hillmyer, M. A., Lipic, P. M., Hajduk, D. A., Almdal, K. & Bates, F. S. (1997). *J. Am. Chem. Soc.* **119**, 2749–2750.
Kamperman, M., Burns, A., Weissgraeber, R., van Vegten, N., Warren, S. C., Gruner, S. M., Baiker, A. & Wiesner, U. (2009). *Nano Lett.* **9**, 2756–2762.
Kamperman, M., Fierke, M. A., Garcia, C. B. W. & Wiesner, U. (2008). *Macromolecules*, **41**, 8745–8752.
Kazimirov, A., Smilgies, D.-M., Shen, Q., Xiao, X., Hao, Q., Fontes, E., Bilderback, D. H., Gruner, S. M., Platonov, Y. & Martynov, V. V. (2006). *J. Synchrotron Rad.* **13**, 204–210.
Kosonen, H., Ruokolainen, J., Torkkeli, M., Serimaa, R., Nyholm, P. & Ikkala, O. (2002). *Macromol. Chem. Phys.* **203**, 388–392.
Lamb, J. S., Cornaby, S., Andresen, K., Kwok, L., Park, H. Y., Qiu, X., Smilgies, D.-M., Bilderback, D. H. & Pollack, L. (2007). *J. Appl. Cryst.* **40**, 193–195.
Lipic, P. M., Bates, F. S. & Hillmyer, M. A. (1998). *J. Am. Chem. Soc.* **120**, 8963–8970.
Meng, Y., Gu, D., Zhang, F., Shi, Y., Cheng, L., Feng, D., Wu, Z., Chen, Z., Wan, Y., Stein, A. & Zhao, D. (2006). *Chem. Mater.* **18**, 4447–4464.
Meng, Y., Gu, D., Zhang, F., Shi, Y., Yang, H., Li, Z., Yu, C., Tu, B. & Zhao, D. (2005). *Angew. Chem. Int. Ed.* **44**, 7053–7059.
Riekel, Ch. (2000). *Rep. Prog. Phys.* **63**, 233–262.
Sinturel, C., Vayer, M., Erre, R. & Heinz Amenitsch, H. (2007). *Macromolecules*, **40**, 2532–2538.
Smilgies, D.-M. (2009). *J. Appl. Cryst.* **42**, 1030–1034.
Wan, Y. & Zhao, D. (2007). *Chem. Rev.* **107**, 2821–2860.
Zhu, L., Cheng, S. Z. D., Calhoun, B. H., Ge, Q., Quirk, R. P., Thomas, E. L., Hsiao, B. S., Yeh, F. & Lotz, B. (2000). *J. Am. Chem. Soc.* **122**, 5957–5967.